



The Effect of O₂ Traces in H₂/H₂O Atmosphere on Oxide Growth on Iron and Crofer 22 APU at 550 and 600 °C

Downloaded from: <https://research.chalmers.se>, 2026-04-17 10:05 UTC

Citation for the original published paper (version of record):

Krogsgaard, T., Svensson, J., Johansson, L. et al (2026). The Effect of O₂ Traces in H₂/H₂O Atmosphere on Oxide Growth on Iron and Crofer 22 APU at 550 and 600 °C. *High Temperature Corrosion of Materials*, 103(2).
<http://dx.doi.org/10.1007/s11085-026-10375-5>

N.B. When citing this work, cite the original published paper.



The Effect of O₂ Traces in H₂/H₂O Atmosphere on Oxide Growth on Iron and Crofer 22 APU at 550 and 600 °C

Thorbjørn Krogsgaard¹ · Jan-Erik Svensson¹ · Lars-Gunnar Johansson¹ · Jan Froitzheim¹

Received: 19 December 2025 / Revised: 20 January 2026 / Accepted: 6 February 2026
© The Author(s) 2026

Abstract

The effect of O₂ traces on the oxidation behavior of iron and a Fe–Cr steel interconnect material (Crofer 22 APU) in a 5% H₂ + 3% H₂O (bal. Ar) environment at 550 and 600 °C has been investigated. The reaction of O₂ with H₂ in the gas at 550 and 600 °C is slow, allowing O₂ traces to reach the samples, despite an excess of H₂ in the gas. Traces of unreacted O₂ resulted in increased oxidation rate as well as hematite formation on iron. The rate of iron oxidation increased with the level of O₂ in the range of 2–550 ppm. The acceleration of oxide growth by O₂ traces is attributed to a greater oxygen activity gradient across the iron oxide scale. To remove O₂ from the gas, a nickel component was positioned upstream from the samples which allowed the gas to equilibrate. Consequently, iron oxidized without hematite formation. Moreover, the use of the nickel component greatly improved the reproducibility of results for both iron and Crofer 22 APU. The use of a catalyst for the O₂ + H₂ reaction in H₂/H₂O exposures proved essential because it provides better control of experimental conditions and thereby more reliable experimental outcomes.

Keywords Interconnect · SOFC · Corrosion · Iron · Low p_{O_2} · Trace O₂

Introduction

Solid oxide fuel cells (SOFCs) and electrolyzer cells (SOECs), collectively known as solid oxide cells (SOCs), have recently attracted increasing scientific and industrial interest due to their potential for highly efficient and low-emission energy conversion [1–4]. SOCs hold substantial commercialization promise, as

✉ Thorbjørn Krogsgaard
thokro@chalmers.se

¹ Department of Chemistry and Chemical Engineering, Chalmers University of Technology, Kemivägen 10, 41296 Gothenburg, Sweden

they can facilitate the production of green electricity and hydrogen, thereby contributing to the decarbonization of hard-to-abate sectors [1, 2].

Achieving the full potential of SOC technology hinges upon reliable operation. Component integrity and longevity, particularly of the cell stack, affect performance and reliability [5–7]. An individual SOC is made up of an anode, a cathode, and an electrolyte [7]. The stack is made by connecting individual cells with a so-called interconnect [8]. The interconnect enables the flow of electrons between the individual cells so that a useful voltage can be produced, as a single cell only offers approximately 0.7 V [8, 9]. Historically, ceramic interconnects have been used, but advancements in the other cell components have allowed operating temperatures to drop from up to 1000 °C to 600–800 °C, which permits the use of more cost-effective metallic interconnect materials [10, 11].

Ferritic stainless steels (FSS) are currently preferred for metallic interconnects due to their cost-effectiveness, machinability, and compatibility with other cell components [12, 13]. Despite these advantages, FSS are known to degrade when exposed to the operating conditions of a SOC, and numerous corrosion phenomena have been observed, such as chromium evaporation, continuous oxide scale growth, and the dual atmosphere effect [13]. All of these phenomena negatively affect SOC performance and can lead to premature cell failure [14–16]. Coatings have been found to alleviate most of the concerns associated with the high pO_2 side, but the low pO_2 side still needs to be better understood [17–19]. Previous studies on the low pO_2 side indicate that, in the 500–800 °C range the most critical corrosion phenomena occur around 600 °C [20, 21]. The oxidation behavior in the 700–800 °C range is better understood compared to oxidation at 600 °C.

Few experimental studies of FSS degradation in H_2/H_2O environment at 600 °C have been published. Also, such experiments are expected to be challenging, e.g., because of relatively slow reaction kinetics in the gas. Therefore, it was deemed necessary to perform a methodological study of the experimental procedure. The present study reports on the influence of traces of unreacted O_2 in a H_2/H_2O gas mixture on experimental outcomes. Experiments were performed on pure iron as well as on the FSS Crofer 22 APU.

Experimental Procedures

Samples

Sheets of 0.3 mm thick Crofer 22 APU (VDM Metals GmbH) and 0.5 mm thick ≥ 99.99 wt.% iron (HMW Hauner GmbH & Co. KG.) were cut into 15 mm \times 15 mm coupons. After cutting, the samples were ultrasonically cleaned at 80 kHz for 10 min in acetone followed by 10 min in ethanol. The samples were then weighed. No further sample preparation was done for Crofer 22 APU. The composition of Crofer 22 APU can be seen in Table 1.

Table 1 Chemical composition of Crofer 22 APU in wt%

Fe	Cr	Mn	Ti	Cu	La	C	S	Si	P	Al
Bal.	22.8	0.45	0.07	0.01	0.08	0.002	<0.002	0.01	0.002	0.01

Further Sample Preparation of Iron

The clean and weighed iron samples underwent a reduction step in a sealed single tube furnace (Entech AB). This process was performed to standardize the samples by reducing any surface oxides and improving bulk purity. The furnace was purged with 5% H₂ (bal. Ar) at a flow rate of 200 mL/min for 1 h before the temperature was ramped from ≈ 50 °C to 1000 °C at a rate of 10 °C/min. The samples were held at 1000 °C for 24 h. Subsequently, the furnace was ramped down to approximately 50 °C, after which the samples were removed. To remove the surface impurities resulting from the thermal treatment, the samples underwent a final polishing sequence using a Tegramin 30 (Struers ApS) automatic polishing machine with, respectively, 1200, 2400, and 4000 grain SiC papers before further polishing with 3 μ m- and 1 μ m diamond suspensions. After polishing, the samples were ultrasonically cleaned and weighed again, following the procedure described previously.

Exposures

System

The experimental setup used is illustrated in Fig. 1. The setup consists of a single tube furnace (Entech AB), a Julabo CORIO CD refrigerated/heating circulator, a three-necked round-bottom flask with coil condenser and heating mantle, metallic

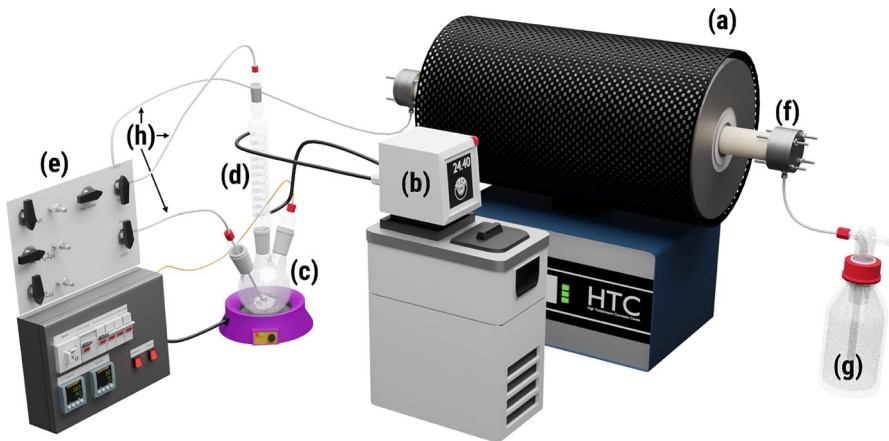


Fig. 1 Experimental setup used to simulate a fuel atmosphere. Labels **a–h** are described in Table 2

tube endcaps, a gas trap, and a temperature-gas control unit. The purpose of different components is described in Table 2. Not shown in Fig. 1 is the 40 mm (L) × 30 (W) mm × 4 mm (H) alumina sample holder used for the exposures. The sample holder has three 40 mm (L) × 0.45 mm (W) × 1 mm (H) slits. All experiments feature triplicate samples, each slit holding one sample. The mass gains reported are average values based on 3 to 21 samples exposed under identical conditions. All gas lines carrying humidified gas to the furnace were wrapped with a heating cord kept at 70 °C and insulated with AF/Armaflex Microban AF-4-010 insulation material. The humidity of the exposure gas was validated with a Michell Optidew Vision optical dew point hygrometer. Different lengths of PTFE tubing were used to introduce a controlled amount of O₂ into the exposure gas upstream of the furnace. Before every experiment the amount of O₂ present in the exposure gas entering the furnace was estimated in the following way: a mixture of 97% N₂ + 3% H₂O was run through the entire exposure system and the level of O₂ in the off-gas was measured by a zirconia sensor (Rapidox 2100 Oxygen Analyser, Cambridge Sensotec Ltd.). Ideally, the measurements should be performed with the experimental gas mixture (5% H₂ + 3% H₂O (bal. Ar)). However, it is not possible to measure trace amounts of O₂ in a H₂/H₂O mixture using a zirconia oxygen sensor. This is because the sensor itself (operating at 650 °C, Pt) catalyzes the reaction between O₂ and excess H₂. Thus, the gas reaches equilibrium inside the sensor, consuming the trace O₂, thereby masking the true *p*O₂ of the gas stream.

Environment

The exposures were performed at 550 °C and 600 °C in a nominally low *p*O₂ atmosphere consisting of 5% H₂ + 3% H₂O (bal. Ar) at a flow rate of 100 sml/min corresponding to ≈ 23 cm/min. To maintain consistency throughout the text, oxygen levels are denoted by *p*O₂ (partial pressure of O₂) rather than the more accurate term, oxygen activity. Before exposure the system was purged with 5% H₂ + 3%

Table 2 Setup explanation

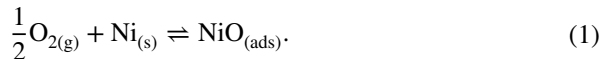
Item	Purpose
Tube Furnace (a)	Tube furnace fitted with a 40 mm I.D. tube made from sintered alumina. The furnace tube is fitted with stainless steel endcaps with O-ring seals.
Circulator (b)	Controls the temperature of the coil condenser (24.4 °C for 3% H ₂ O).
Three-necked flask (c)	Water container kept at 30 °C. The exposure gas is humidified before going to the coil condenser.
Coil-condenser (d)	The coil condenser is used to accurately set the dew point of the humidified gas.
Control Unit (e)	Sets the desired gas type and flow. Controls the temperature ramping and set points of the furnace and the heating mantle.
Endcaps (f)	Hermetically seals the alumina tube from the surrounding atmosphere.
Gas Trap (g)	Creates a water seal allowing gas to leave the furnace but not enter.
PTFE Tubing (h)	Used for gas transport. Later changed to AISI316L steel tubing. All gas lines carrying humidified gas to the furnace were wrapped with a heating cord kept at 70 °C.

H₂O (bal. Ar) at 1000 sml/min for 30 min and for > 16 h at 100 sml/min. Temperature was ramped with 23 °C/min. The samples were furnace-cooled approximated as $510.65e^{-0.003x}$ where x is time in minutes and 510.65 a temperature controller value. To avoid condensation, the samples were removed when the temperature reached 50 °C.

Catalyst and Oxygen Getter

To remove traces of unreacted O₂ from the gas, a nickel component was positioned upstream from the samples, allowing the gas to equilibrate. The component was fabricated from ≥99.99 wt% nickel and consisted of an array of staggered, parallel, tubes (0.5 mm wall thickness) providing a total surface area of 209 cm². Figure 2a shows the geometry of the nickel component. Figure 2b is a schematic of the furnace tube showing the location of the nickel component relative to the samples. Under isothermal conditions, the temperature of the nickel component was within 50 °C of the sample temperature.

Nickel oxidation is not spontaneous in the nominal (equilibrated) experimental gas (5% H₂ + 3% H₂O (bal. Ar)). Yet, traces of O₂ present in the actual, non-equilibrium, gas are expected to react with nickel. Thus, O₂ is known to react rapidly with nickel, both at room temperature and elevated temperature, undergoing dissociative chemisorption and charge transfer to form oxide [22, 23]:



In an oxidizing environment, absent from H₂, Eq. 1 is followed by nucleation of NiO_(s) on the surface [22, 23]. In the present case, the gas has a large excess of H_{2(g)} which is reported to form highly mobile atomic hydrogen on the nickel surface [24]:

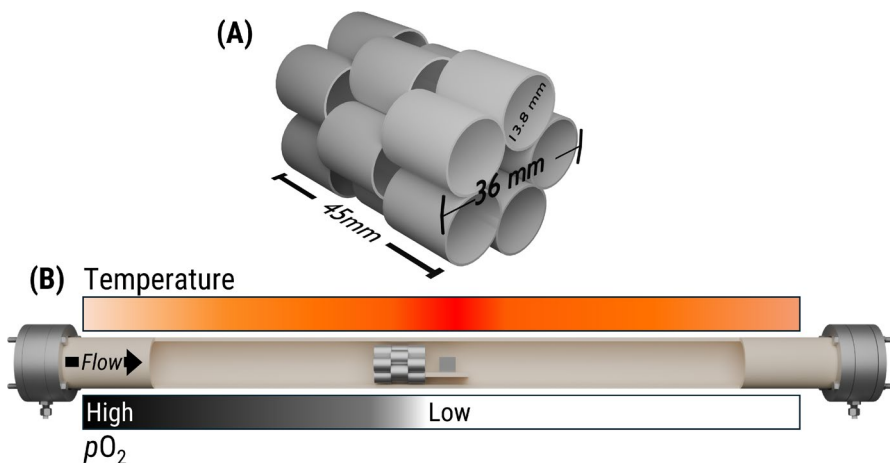
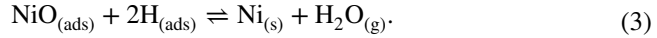


Fig. 2 a Geometry of the nickel component. b Schematic of the furnace tube with the nickel component and samples

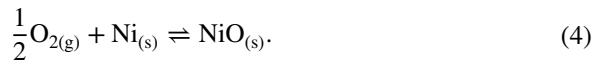


Adsorbed hydrogen is reported to react rapidly with $\text{NiO}_{(\text{s})}$ at $>250\text{ }^\circ\text{C}$ to form $\text{Ni}_{(\text{s})}$ and $\text{H}_2\text{O}_{(\text{g})}$ [25]. In the present case it is suggested that NiO reacts already in the adsorbed state:



This scenario (Eqs. 1–3) is in line with reports showing Ni/NiO systems effectively catalyzes the reaction between O_2 and H_2 [26–28]. During the experiments no decrease in efficiency of the nickel component was observed.

Because of the rapid reaction between O_2 and nickel, the nickel component is also an efficient O_2 getter in oxidizing conditions (in the absence of H_2) at high temperatures:



The efficiency of the nickel component as an O_2 getter was confirmed in experiments at $600\text{ }^\circ\text{C}$ in $97\%\text{ N}_2 + 3\%\text{ H}_2\text{O}$ and in $100\%\text{ N}_2$. The tests were run with a gas flow of 100 sml/min and a temperature ramp of $\approx 22\text{ }^\circ\text{C/min}$.

Figure 3 illustrates the $p\text{O}_2$ measured at the furnace outlet. In a system configured with minimized levels of trace O_2 and in the absence of the nickel component the system maintained a stable baseline of 3 ppm O_2 in dry N_2 .

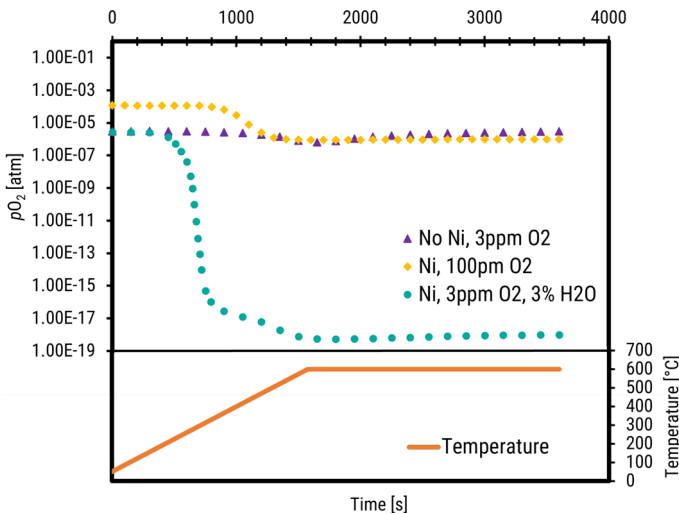
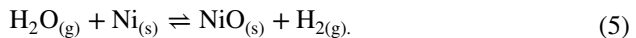


Fig. 3 $p\text{O}_2$ downstream of the furnace with and without the nickel component. The legend refers to the $p\text{O}_2$ before the gas enters the system. In dry $100\%\text{ N}_2$ with initial 100 ppm O_2 , the component reduced $p\text{O}_2$ from 10^{-4} to 10^{-6} atm, whereas in $97\%\text{ N}_2 + 3\%\text{ H}_2\text{O}$, a lower equilibrium $p\text{O}_2$ of $\sim 10^{-18}$ atm was achieved

To evaluate the gettering performance, a controlled amount of O_2 was introduced, establishing a measured pO_2 of 100 ppm (10^{-4} atm) for the cold system. After reaching approximately 400 °C, the nickel component functioned as an O_2 getter, reducing the pO_2 in the output gas from 10^{-4} atm to a stable level of $\approx 10^{-6}$ atm. Tests performed at various initial O_2 levels consistently converged to this same pO_2 value, suggesting that $\approx 10^{-6}$ atm represents the experimental lower limit under these conditions. The lower limit is likely bounded by either the component's kinetics as a getter or the sensor's detection capabilities. In contrast, exposure to a humidified atmosphere (97% N_2 + 3% H_2O) resulted in a markedly lower equilibrium pO_2 of approximately 10^{-18} atm.

The much lower pO_2 in the humid environment is attributed to the reduction of water by nickel:



The signal from the oxygen sensor corresponds to the equilibrium H_2/H_2O ratio generated by Eq. 5; see Fig. 3. The equilibrium concentration of H_2 generated by Eq. 5 is ≈ 300 ppm.

Analysis

Gravimetric analysis was performed by weighing the samples before and after exposure on a Mettler Toledo XP6 microbalance. A Leica EM TIC 3X Broad Ion Beam mill was used to prepare cross sections and a JEOL JSM-7800F Prime SEM equipped with an Oxford Instruments Energy-Dispersive X-ray spectrophotometer was used for the analysis of microstructure and chemical analysis. X-ray diffraction was carried out with a Bruker D8 Discovery in Bragg–Brentano geometry with $Mo\ k_\alpha$ radiation (0.7093 Å) to detect crystalline phases formed. Optical analysis was used to estimate oxide type, oxide coverage, and severity of corrosion.

Results and Discussion

Initial 600 °C Results

The initial exposures of Crofer 22 APU at 600 °C resulted in mass gains of 1.06 ± 0.32 mg/cm² after 24 h and 1.11 ± 0.12 mg/cm² at 168 h, respectively (Fig. 4). This can be contrasted with previous results from this lab by Alnegren et al. [29] for a similar alloy, Crofer 22H at 850 °C, using the same experimental setup and the same nominal gas composition. Alnegren et al. [29] reported 0.15 ± 0.01 mg/cm² and 0.32 ± 0.02 mg/cm² after 24 and 168 h, respectively; see Fig. 4. High mass gains have been reported previously for FSS in H_2/H_2O environments at 600 °C, due to the formation of non-protective oxides. Conversely, higher temperatures favor the formation of protective chromia scales [20, 21, 30]. However, the lack of reproducibility at 600 °C seen in Fig. 4 is particularly striking.

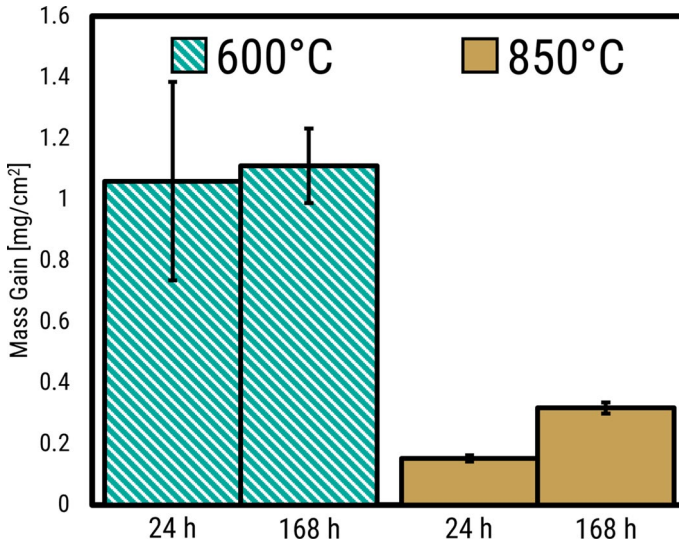


Fig. 4 Mass gains for Fe22Cr steels exposed at 600 °C and 850 °C in 5% H₂ + 3% H₂O (bal. Ar). The data at 600 °C refer to Crofer 22 APU while the 850 °C dataset is from [29] on Crofer 22H. From an oxidation point of view, the materials are highly similar. Error bars represent the standard deviation

To investigate the causes behind the relatively poor reproducibility at 600 °C, pure iron was investigated under the same exposure conditions and using the same experimental setup. While iron is not suitable as an interconnect material pure iron was selected to elucidate this issue because its oxidation behavior is fundamentally simpler compared to the oxidation of Crofer 22 APU. Figure 5 shows mass gains recorded after exposures performed with three identical furnaces and in multiple runs; each bar represents one sample. Figure 5 shows a large variation between different furnaces but also for the same furnace. The scatter in results between different runs and also between furnaces is significant and indicates that there is a problem with the exposure environment.

Since the Alnegren et. al. data prove that the system is capable of reproducibility, two scenarios were hypothesized to have caused reproducibility issue. The first hypothesis being that the exposure gas does not fully equilibrate at 600 °C as opposed to at 850 °C. The experimental gas upstream from the hot zone in the furnace contains traces of O₂ which are expected to react with H₂ at high temperature, forming water. However, at intermediate temperatures, when the reaction is slower, the gas reaching the samples may contain small amounts of O₂. Also, the level of O₂ reaching the samples would vary, depending both on the position in the furnace and between runs. The non-equilibrated gas hypothesis is supported by XRD (not shown) which confirms the presence of hematite on both Crofer 22 APU and iron samples exposed at 600 °C. For hematite to be stable at 600 °C, a p_{O_2} of approximately 10^{-14} atm is required but the theoretical p_{O_2} for 5% H₂ + 3% H₂O (bal. Ar) at 600 °C is 4.6×10^{-25} atm; see Table 3. The presence of hematite thus proves significant local variations in p_{O_2} .

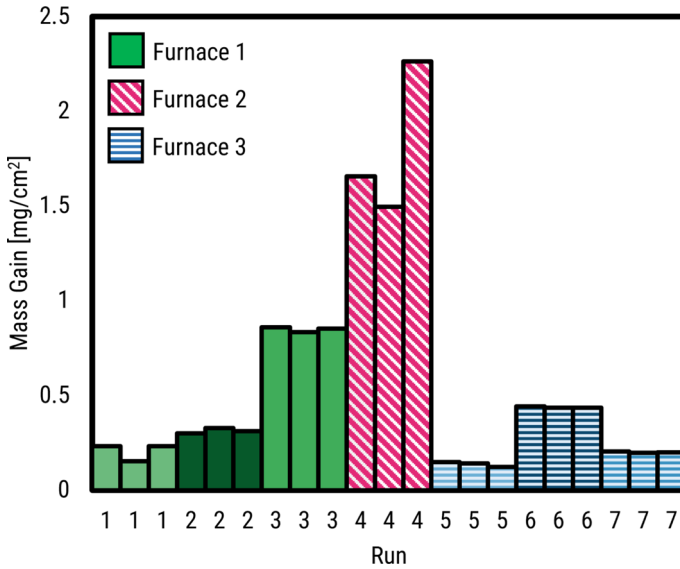


Fig. 5 Iron samples exposed to 5% H₂ + 3% H₂O (bal. Ar) at 600 °C for 24 h. Results from three identical furnaces and for multiple runs are shown

Table 3 Equilibrium *p*O₂ in 5% H₂ + 3% H₂O (bal. Ar) at 550 °C and 600 °C as well as dissociation pressures for iron oxides. Calculations were made using data sourced from [31]

	550 °C	600 °C
5%H ₂ / 3%H ₂ O	7.6 x 10 ⁻²⁷ atm	4.6 x 10 ⁻²⁵ atm
Fe _{0.947} O/Fe	N.A.	1.48 x 10 ⁻²⁵ atm
Fe ₃ O ₄ /Fe	1.55 x 10 ⁻²⁷ atm	N.A.
Fe _{0.947} O/Fe ₃ O ₄	N.A.	1.54 x 10 ⁻²⁵ atm
Fe ₃ O ₄ /Fe ₂ O ₃	1.76 x 10 ⁻¹⁶ atm	0.90 x 10 ⁻¹⁴ atm

The second hypothesis concerns wüstite formation. Wüstite is just stable, thermodynamically, under the experimental conditions (see Table 3), and since the growth rate of wüstite is high compared to magnetite, the scatter in the results could be due to a difference in early wüstite formation on the surface. A variation between samples in the nucleation of wüstite during early exposure is expected to result in mass gain variations. The problem would be accentuated by the relatively short exposure time of 24 h. Figure 6 shows the cross section of one of the iron samples. XRD (not shown) confirms the presence of hematite, magnetite, and wüstite. Below 570 °C wüstite undergoes eutectoid decomposition into a mixture of α-Fe and magnetite. Partial decomposition of wüstite happens during cooling, giving rise to a characteristic microstructure seen in Fig. 6. The ratio of wüstite to the other oxides is roughly four to one which illustrates the fact that wüstite formation plays an outsize role with regards to early mass gains. To test whether wüstite formation is causing the large fluctuations in mass gain at

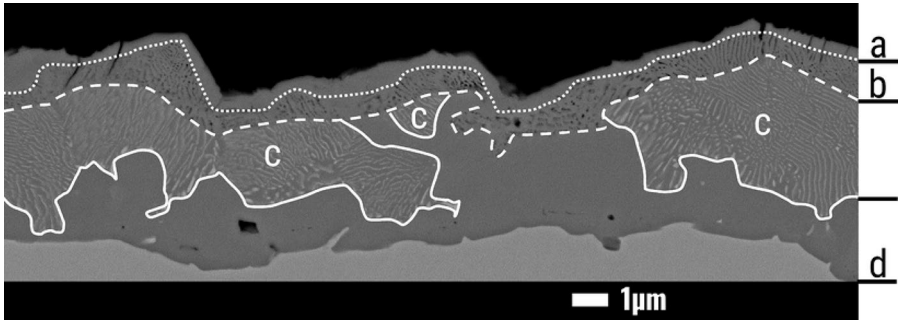


Fig. 6 SEM cross section image of the oxide scale formed on iron after 24 h in 5% H₂ + 3% H₂O (bal. Ar) at 600 °C. No attempt was made to remove or reduce O₂ traces of the input gas for this exposure. The different scale constituents are indicated: **a** hematite, **b** magnetite, **c** eutectoid magnetite + α -Fe, **d** Wüstite. The white lines mark the regions of different oxides and only acts as a visual aid to help separate the oxide phases

600 °C, additional experiments were conducted at 550 °C, below the phase stability field of wüstite.

Iron 550 °C Results

The iron samples exposed at 550 °C, with a high level of O₂ present, showed a red discoloration; see Fig. 7. The optical images in Fig. 7 show that the direction of gas flow has a major effect on oxide morphology. Thus, the leading edge of the samples shows a red discoloration while the middle and downstream parts exhibit different shades of gray. Figure 7a and b shows cross sections of the oxide scales from the gray and red areas, respectively. The oxide thickness is about 5 μ m in the former case and 7 μ m in the latter. These oxide thicknesses are in good agreement with the observed mass gains considering an oxide scale consisting of hematite and magnetite. The SEM top-view images in Fig. 7(c-g) show a high density of needle-like crystallites in the red regions while the number density of needles is much lower in the gray areas. The red color and the needle-like crystallites indicate hematite. However, the p_{O_2} corresponding to equilibrium in the exposure gas, $p_{O_2} = 7.6 \times 10^{-27}$ atm, is far below the level which allows hematite formation, 1.76×10^{-16} atm at 550 °C. Hence, the exposure gas cannot be at equilibrium if hematite is present. The leading-edge effect seen as the color changes from red to gray is in addition a “smoking gun” for the presence of trace levels of highly reactive contaminants (i.e., O₂) in the flowing gas. This all implies that the reaction of H₂ with traces of O₂ entering the furnace is not sufficiently fast to eliminate the effect of O₂ on the samples and avoid hematite formation.

Improved control of trace O₂ in the gas supply was achieved by replacing all PTFE tubing with stainless steel tubing. This lowered the O₂ concentration in the input gas to 2–3 ppm. To investigate how the level of O₂ in the upstream gas affects iron oxidation, a series of experiments were performed where a controlled amount of O₂ was added to the experimental gas. It was observed that, under ambient

conditions, 1 m of $\varnothing 6$ mm PTFE tubing led to a stable permeation rate of $\approx 3.5 \times 10^{-8}$ moles of O_2 per minute (9 ppm O_2 per meter PTFE tubing) from the ambient air into the exposure gas. These values match well with the literature values for the O_2 permeability of PTFE [32, 33]. Based on this finding, pre-decided levels of O_2 in the input gas were achieved by including a measured length of PTFE tubing into the humidifier part of the setup.

Figure 8 illustrates the effect of O_2 traces in the input gas, in the range 2.5–550 ppm, on mass gain, revealing a strong correlation between oxide growth and the O_2 level. Due to how the O_2 levels were determined, see Sect. 2.2, the values presented are indicative rather than exact. However, there is nothing to suggest a change in the O_2 permeation rate when the gas changes to 5% H_2 + 3% H_2O (bal. Ar) from 97% N_2 + 3% H_2O .

The mass gain which was 0.07 mg/cm^2 at 2.5 ppm O_2 increased by a factor of four when the O_2 concentration in the input gas was raised to 20 ppm. The large scatter in mass gain observed at 550 ppm O_2 is attributed to local non-uniformities in the gas stream. At this concentration, high reactivity leads to a decrease in the O_2 concentration as the gas flows over the samples, resulting in the leading-edge effect seen in Fig. 7.

The strong dependence of mass gain on the O_2 level in the upstream gas shows that iron oxidation is strongly influenced by the traces of O_2 that reach the samples due to incomplete equilibration of the gas. The presence of O_2 traces at the sample surface is expected to dramatically increase the pO_2 at the gas/oxide interface compared to a situation where water is the only oxidant. This will result in a correspondingly greater driving force for oxidation, explaining both the faster oxide growth with increasing levels of upstream- O_2 , and the appearance of hematite. Furthermore, the situation changes from H_2O being the only oxidant to a situation where O_2 is expected to be the main oxidant. This shows that at intermediate temperatures even trace amounts of O_2 can have an outside impact on the corrosion rate.

As it is challenging to consistently ensure such low levels of O_2 for a system in daily use, it was decided to investigate the effect of an O_2 catalyst/getter. The utilized catalyst/getter is made from nickel and is placed in the furnace tube, upstream from the samples. Nickel was selected for this application because of its catalytic properties, reactivity with oxygen, and thermodynamic stability in the exposure gas, as well as its wide availability. Henceforth, the nickel catalyst/getter will be designated as the nickel component. A sample exposed at 550 ppm O_2 with the nickel component is shown in Fig. 9. The exposures with the nickel component resulted in a well adherent, dense oxide with a thickness of around $0.6 \mu\text{m}$; see Fig. 9a. Further, comparing the top-view image in Fig. 9b with the top views from the exposure without the nickel component in Fig. 7c–g shows a more uniform oxide in the former case. The mass gains measured for the iron samples exposed with various levels of deliberately added trace O_2 while utilizing the nickel component are shown in Fig. 9c. In Fig. 9c, the data points representing the nickel component exposures are positioned along the horizontal axis according to the concentration of O_2 in the gas entering the furnace, measured as described in Sect. 2.2. The position on the x-axis is therefore not representative of the atmosphere experienced by the samples in those exposures. The results in Fig. 9c clearly show that with the nickel component upstream, the

Fig. 7 SEM imaging of iron after 24 h in 5% H₂ + 3% H₂O (bal. Ar) at 550 °C with 550 ppm of O₂. At the top are optical images showing leading-edge behavior. The optical images also show the location of a–g on the sample. a, b are cross-sectional electron images from two different regions of the sample. c–g are top-view electron images

gas effectively equilibrates so that even a high O₂ contamination of 550 ppm in the upstream gas has no effect on the oxidation rate of iron. Figure 9c further shows that the mass gains achieved at 2.5 ppm without the nickel component are similar to the mass gains achieved with the nickel component. The mass gain plateau at low levels of upstream-O₂ indicates that the rate of reaction between O₂ and H₂ is sufficiently fast to reduce the level of O₂ reaching the samples to a point

where it does not influence oxide growth. An experiment using a platinum catalyst at 550 ppm O₂ produced results indistinguishable from those achieved with the nickel component (Fig. 9c).

The difference in oxidation behavior apparent from a comparison of Figs. 7 and 9 shows that the nickel component had a significant effect on oxidation behavior. Accordingly, XRD analysis (Fig. 10) confirms the presence of hematite (e.g., peak at $2\theta=15^\circ$) on samples exposed to the experimental gas mixture (5% H₂ + 3% H₂O (bal. Ar)) when the input O₂ concentration was ≥ 19 ppm. In contrast, hematite was not detected at about 2 ppm O₂ in the input gas. Furthermore, when the nickel component was utilized no hematite was detected even with a high level of 550 ppm O₂ in the input gas.

Revisiting 600 °C

Based on the experience gained from the exposures of iron at 550 °C, see Sect. 3.2, exposures of iron and Crofer 22 APU were repeated at 600 °C. The aim was to assess whether the poor reproducibility seen in Figs. 4 and 5 could be improved by introducing the nickel component, thereby minimizing the influence of trace O₂.

Iron at 600 °C Revisited

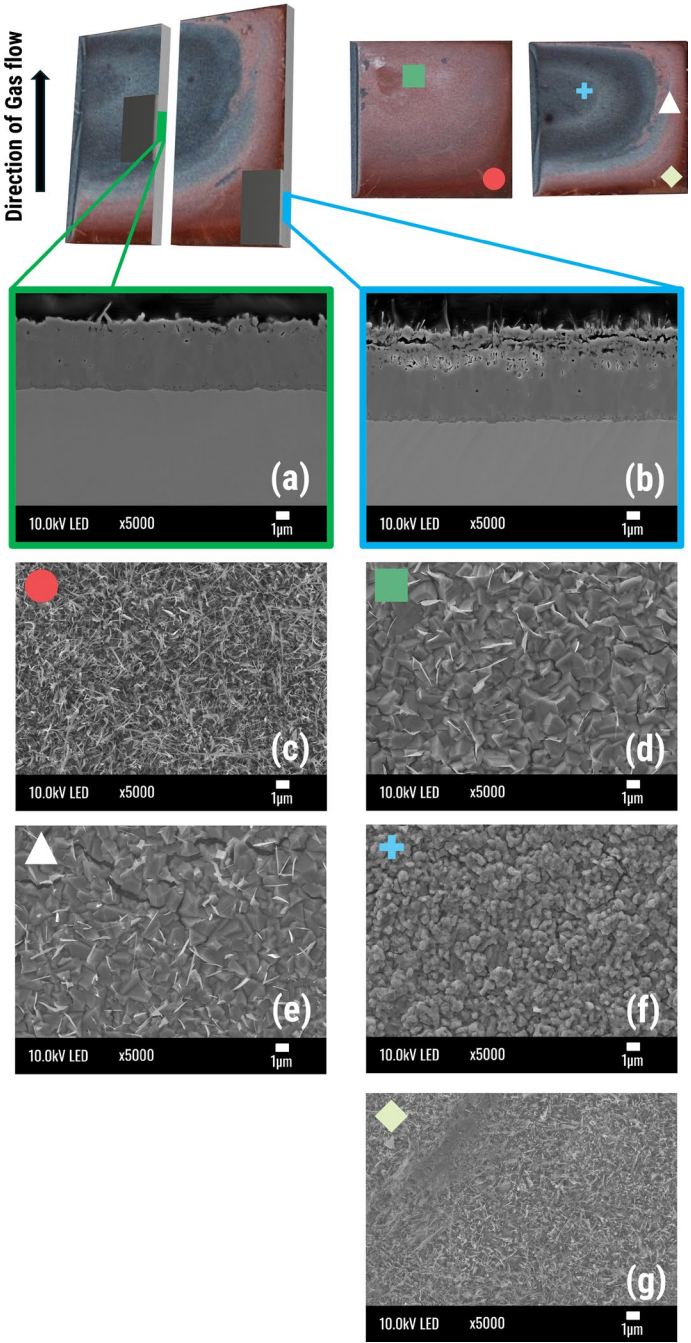
The influence of removing trace O₂ from the input gas on the mass gain of iron at 600 °C in 5% H₂ + 3% H₂O (bal. Ar) is shown in Fig. 11. The results demonstrate a pronounced decrease in mass gain and a significant reduction in data scatter. Previously, the average mass gain after 24 h was 0.56 ± 0.56 mg/cm², whereas after removal of trace O₂ it decreased to 0.09 ± 0.04 mg/cm². The high reproducibility indicates that the large mass gain scatter measured initially at 600 °C is due to O₂ traces in the gas and not to wüstite formation.

Crofer 22 APU at 600 °C Revisited

The reduction in trace O₂ also affected Crofer 22 APU at 600 °C in 5% H₂ + 3% H₂O (bal. Ar), as shown in Fig. 12. The high mass gain of Crofer 22 APU compared to iron is interesting and the oxidation behavior of FSS under low-*p*O₂ conditions

Cross-Sections

Top-View



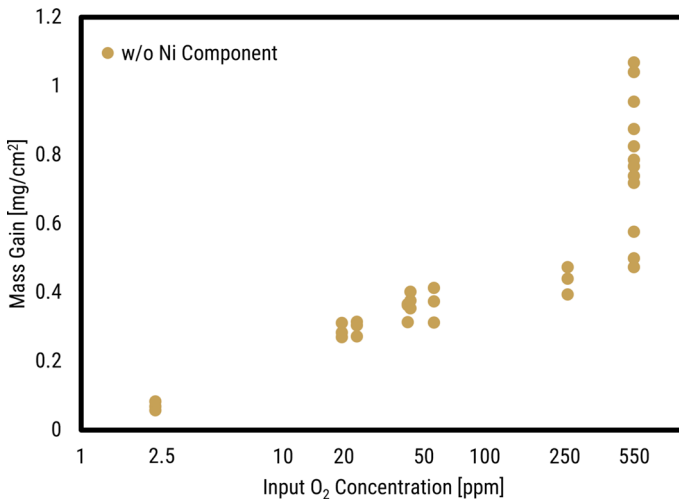


Fig. 8 Effect of different trace O₂ levels in the input gas on the mass gain of iron after 24 h in 5% H₂ + 3% H₂O (bal. Ar) at 550 °C in the absence of the nickel component. Each point represents a sample. The input O₂ concentration was measured in 97% N₂ + 3% H₂O. (w/o = without)

will be further investigated. However, for the present study, it is important to note that both the mass gain and scatter were reduced after 24 and 168 h of exposure, although the effect was less pronounced than for pure iron. The recorded mass gains remain considerably higher than those reported for Crofer 22H at 850 °C.

The mass gain data collected with the nickel component (Figs. 11 and 12) show both lower average mass gains and improved reproducibility, indicating that the large scatter observed in earlier 600 °C experiments was largely due to variations in trace O₂ reaching the samples. Hence, due to the relatively slow gas-phase reaction between O₂ and H₂, trace amounts of O₂ in the input gas can reach the samples and thereby exert a significant influence on the oxidation behavior. Importantly, the present findings show that the trace O₂ problem can be effectively alleviated through the use of an O₂ catalyst/getter, such as the nickel component, even when the input gas contains comparatively high oxygen levels. These findings should be applicable to oxidation studies at intermediate temperatures under low-*p*O₂ conditions for a wide range of materials such as austenitic steels, nickel-based alloys, as well as other FSS.

Conclusions

Oxide growth on iron and on Crofer 22 APU in a simulated SOC H₂/H₂O environment at 600 °C is strongly influenced by a few ppm of O₂ in the exposure gas reaching the samples. Meticulous control of oxygen levels is therefore necessary.

- The oxidation of pure iron at 550 °C in a 5% H₂ + 3% H₂O (bal. Ar) environment is profoundly influenced by ppm levels of O₂. The oxide growth rate was

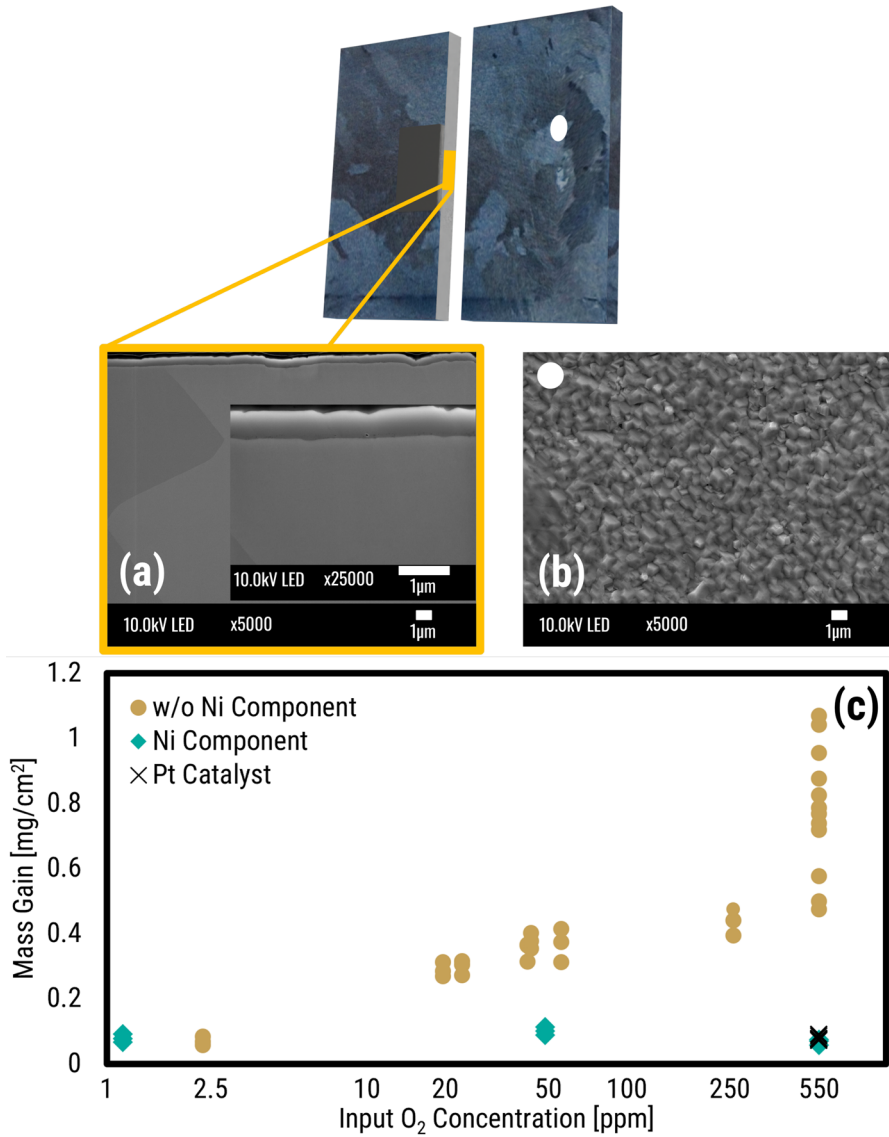


Fig. 9 Iron samples exposed at 550 °C for 24 h in 5% H₂ + 3% H₂O (bal. Ar) with different trace O₂ levels, in the presence of the nickel component. The top optical image shows the location of images (a) and (b). **a** Is a SEM cross section of the scale, **b** is a top-view SEM image, **c** mass gain as a function of the concentration of O₂ in the input gas in the presence of the nickel component/platinum catalyst. Data points from Fig. 8 are included for comparison. The input O₂ concentration was measured in 97% N₂ + 3% H₂O (w/o = without)

found to be directly correlated with the O₂ concentration in the input gas. The O₂ traces increase the oxidizing potential at the gas/oxide interface, as evidenced by the formation of hematite. Consequently, the larger resulting oxy-

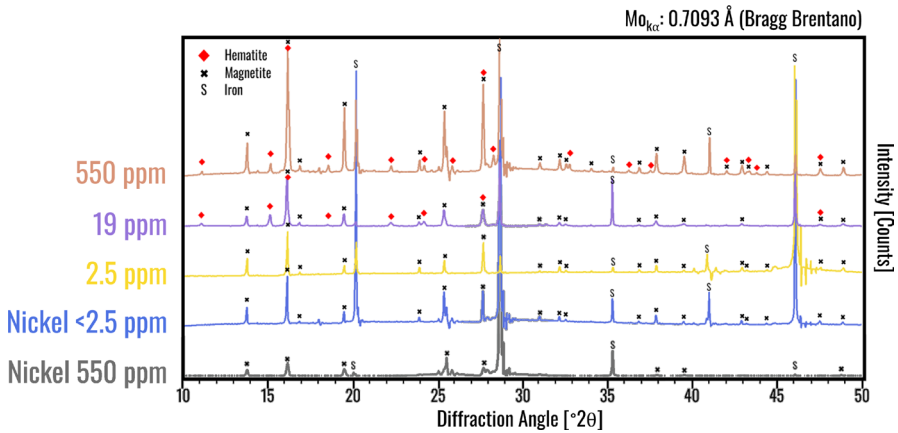


Fig. 10 XRD diffractograms showing the presence of hematite down to 19 ppm O_2 for samples exposed to 5% H_2 + 3% H_2O (bal. Ar) at 550 °C for 24 h. The listed ppm levels refer to O_2 in the furnace input gas. The "Nickel" label indicates that a nickel component was present in the experiment

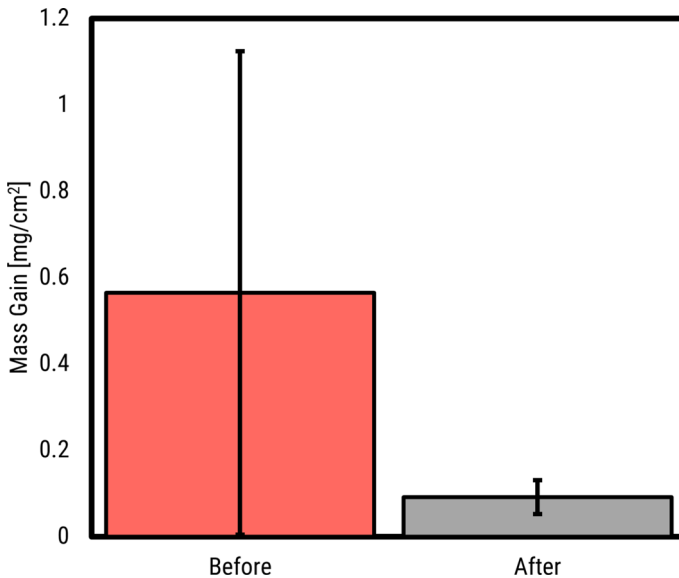


Fig. 11 Side-by-side comparison of the mean mass gain values recorded on iron at 600 °C for 24 h in 5% H_2 + 3% H_2O (bal. Ar) with the nickel component (After) and without it (Before). Error bars represent the standard deviation

gen potential gradient across the oxide layer leads to significantly accelerated oxide growth compared to an environment free from trace O_2 .

- Similarly, trace O_2 levels were found to influence oxide growth on Crofer 22 APU at 600 °C in H_2/H_2O environments mimicking SOC fuel-side condi-

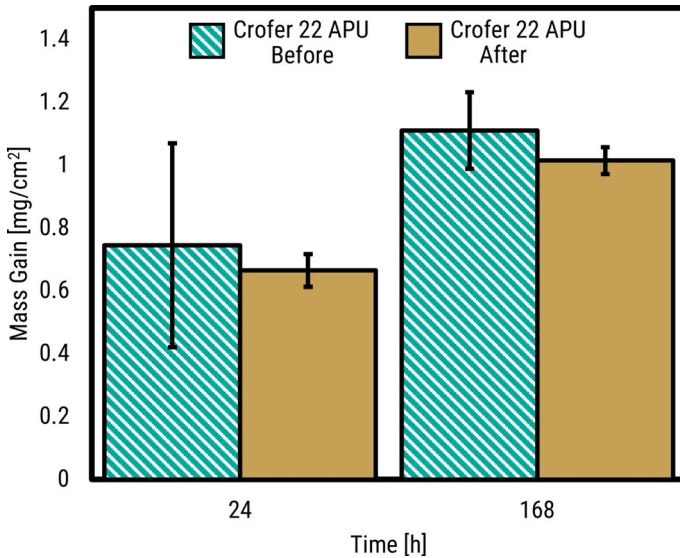


Fig. 12 Side-by-side comparison of the mean mass gain of Crofer 22 APU at 600 °C for 24 h and 168 h in 5% H₂ + 3% H₂O (bal. Ar). "Before" data collected with the original experimental setup. "After" data collected with the updated system (minimized trace O₂ contamination and with the nickel component). Error bars represent the standard deviation

tions. This influence was observed to have a detrimental effect on experimental reproducibility.

- An O₂ catalyst/getter fabricated from nickel demonstrated high efficiency in removing trace O₂ from both the experimental gas (5% H₂, 3% H₂O, bal. Ar) and from dry N₂. The application of this nickel component resulted in significantly improved reproducibility for oxidation experiments in the H₂/H₂O environment, a benefit observed for both pure iron (at 550 °C and 600 °C) and for Crofer 22 APU (at 600 °C).
- A method is presented enabling the introduction of well-controlled trace amounts of O₂ to an experimental gas using PTFE tubing.

Acknowledgments This work was carried out within the Swedish High Temperature Corrosion Centre (HTC) at Chalmers University of Technology. Elcogen Oy is acknowledged for supplying Crofer 22 APU.

Author Contributions TK contributed with method development, experimental work, writing—original draft, writing—review and editing, visualization. JS and LJ contributed to conceptualization, writing—review and editing. JF contributed to conceptualization, supervision, writing—review and editing.

Funding Open access funding provided by Chalmers University of Technology. Funding provided by Sweden's Innovation Agency Vinnova and the Swedish energy agency through the "Fordonstrategisk Forskning och Innovation" (FFI) project.

Data Availability All data supporting the findings of this study are available upon request to the corresponding author.

Declarations

Conflict of interest The authors declare no competing interests.

Open Access This article is licensed under a Creative Commons Attribution 4.0 International License, which permits use, sharing, adaptation, distribution and reproduction in any medium or format, as long as you give appropriate credit to the original author(s) and the source, provide a link to the Creative Commons licence, and indicate if changes were made. The images or other third party material in this article are included in the article's Creative Commons licence, unless indicated otherwise in a credit line to the material. If material is not included in the article's Creative Commons licence and your intended use is not permitted by statutory regulation or exceeds the permitted use, you will need to obtain permission directly from the copyright holder. To view a copy of this licence, visit <http://creativecommons.org/licenses/by/4.0/>.

References

1. F. Gniewomir, Solid oxide electrolysis: A technology status assessment, Clean Air Task Force, Tech. Rep., 2023. Accessed 22 Sep. 2025. <https://cdn.catf.us/wp-content/uploads/2023/11/15092028/solid-oxide-electrolysis-report.pdf>.
2. T. Amit, C. Amrit, S. Pranjali, et al., *The Scientific World Journal* 2024. <https://doi.org/10.1155/2024/6443247>.
3. Solid oxide electrolysis cell (soec) market size, share, growth, and industry analysis ... forecast to 2033. <https://www.marketgrowthreports.com/market-reports/solid-oxide-electrolysis-cell-soec-market-112615>. Accessed 22 Sep. 2025.
4. V. Marcantonio and L. Scopel, *Sustainability* **16**, 2024 (10773). <https://doi.org/10.3390/su162310773>.
5. Q. Ma, Y. Zuo, K. Lu, et al. *Inorganics* **12**, 2024 (288). Accessed 2024; discusses degradation mechanisms in SOEC under cycling/steady operation. <https://doi.org/10.3390/inorganics12110288>.
6. M. Kindelmann, O. Guillon, J. Mayer, N. Menzler, *Journal of Materials Chemistry A* 2025. <https://doi.org/10.1039/D5TA03917G>.
7. M. Lang, P. Szabo, R. Costa, et al., *Journal of The Electrochemical Society* **170**, 2023 (114). Reversible cycling, SOC stacks; quantifies performance degradation over time. <https://doi.org/10.1149/1945-7111/ad09f3>.
8. Q. Fu, A. Brisse, S.D. Iorio, et al., "Socetsqa tm 00: General soc testing guidelines-solid oxide cell and stack testing, safety and quality assurance," EU FP7 Project SOCTESQA (Grant Agreement No. 621245), FCH JU, Tech. Rep. Version 2.5, May 2017, "General SOC Testing Guidelines", test module TM 00. https://elib.dlr.de/119897/1/tm00_general_for-d3.6.pdf.
9. J. Larminie and A. Dicks, *Fuel Cell Systems Explained*, 2nd ed (Wiley, New York, 2003),.
10. M. Fellet, W. Rossner, *MRS Bulletin* **40**, 2015 (742). Discusses original SOFC temps of 800–1000°C and temperature lowering to enable metallic interconnects. <https://link.springer.com/article/10.1557/mrs.2015.35>.
11. Z. Yang, *International Materials Reviews*. **53**, 2008 (39). States that with SOFC operating temp 650–800°C, metallic interconnects become viable. <https://doi.org/10.1179/174328007X212526>.
12. T.L. Skafte, J. Hjelm, P. Blennow, C.R. Graves, Quantitative review of degradation and lifetime of solid oxide cells and stacks, in *Proceedings of European SOFC & SOE Forum (SOFC-XIV)*, Includes "choice of materials" trends, showing improvements in degradation rates connected with better interconnects, including metallic ones, 2020. <https://orbit.dtu.dk/en/publications/quantitative-review-of-degradation-and-lifetime-of-solid-oxide-ce>.
13. J. W. Fergus, *Materials Science and Engineering A* **397**, 2005 (271). <https://doi.org/10.1016/j.msea.2004.12.074>.
14. W. J. Quadackers, H. Greiner, M. Zahid, and L. Singheiser, *Materials at High Temperatures* **20**, 2003 (115). <https://doi.org/10.1179/mht.2003.015>.

15. J. Mao, W. Yuan, H. Li, Y. Wang, H. Sun, and H. Dong, *RSC Advances* **14**, (14), 2024 (8831). <https://doi.org/10.1039/D3RA08424H>.
16. P. Alnegren, J. Froitzheim, and J.-E. Svensson, *Journal of Power Sources* **387**, 2018 (118). <https://doi.org/10.1016/j.jpowsour.2018.03.033>.
17. M. T. Tomas, J.-E. Svensson, and J. Froitzheim, *International Journal of Hydrogen Energy* **58**, 2024 (852). <https://doi.org/10.1016/j.ijhydene.2024.01.219>.
18. M. T. Tomas, A. Visibile, J.-E. Svensson, and J. Froitzheim, *International Journal of Hydrogen Energy* **48**, 2023 (18405). <https://doi.org/10.1016/j.ijhydene.2023.01.313>.
19. M. Reddy, J. Froitzheim, J.-E. Svensson, Reevaluating the cr evaporation characteristics of ce/co coatings for interconnect applications, in *Proceedings of the 17th International Symposium on Solid Oxide Fuel Cells (SOFC 2021), Shows that Ce/Co Coatings Greatly Reduce Cr Evaporation from Interconnect Steel at SOFC Operating Conditions*, 2021, pp. 1899. <https://doi.org/10.1149/10301.1899ecst>.
20. K. O. Gunduz, A. Chyrkin, C. Goebel, et al., *Corrosion Science* **179**, 2021 (109). <https://doi.org/10.1016/j.corsci.2020.109112>.
21. A. Chyrkin, K. O. Gunduz, V. Asokan, J.-E. Svensson, and J. Froitzheim, *Corrosion Science* **203**, 2022 (110). <https://doi.org/10.1016/j.corsci.2022.110338>.
22. F. Besenbacher and J. K. Nørskov, *Progress in Surface Science* **44**, 1993 (5). [https://doi.org/10.1016/0079-6816\(93\)90006-H](https://doi.org/10.1016/0079-6816(93)90006-H).
23. K. Kanhaiya and H. Heinz, *Nano Letters* **22**, 2022 (5392). <https://doi.org/10.1021/acs.nanolett.2c00490>.
24. A. A. Pisarev, Hydrogen adsorption on the surface of metals," in *Gaseous Hydrogen Embrittlement of Materials in Energy Technologies, ser. Woodhead Publishing Series in Metals and Surface Engineering*, R. P. Gangloff and B. P. Somerday, Eds., vol. 1, Woodhead Publishing, 2012, pp. 3. <https://doi.org/10.1533/9780857095374.1.3>.
25. J. A. Rodriguez, J. C. Hanson, A. I. Frenkel, J. Y. Kim, and M. Pérez, *Journal of the American Chemical Society* **124**, 2002 (346). <https://doi.org/10.1021/ja0121080>.
26. Y. Dong, J. Dang, W. Wang, S. Yin, and Y. Wang, *ACS Applied Materials and Interfaces* **10**, 2018 (39624). <https://doi.org/10.1021/acsami.8b12573>.
27. A. Oshchepkov, A. Bonnefont, and E. Savinova, On the influence of the extent of oxidation on the kinetics of the hydrogen electrode reactions on polycrystalline nickel. *Electrocatalysis* **11**, 2020 (133–142). <https://doi.org/10.1007/s12678-019-00560-3>.
28. Z. Zhou, Y. Liu, J. Zhang, H. Pang, and G. Zhu, *Electrochemistry Communications* **121**, 2020 (106). <https://doi.org/10.1016/j.elecom.2020.106871>.
29. P. Alnegren, Corrosion of ferritic stainless steel interconnects for solid oxide cells-challenging operating conditions. Ph.D. dissertation, Chalmers University of Technology, Gothenburg, Sweden, 2018. https://research.chalmers.se/publication/503125/file/503125_Fulltext.pdf.
30. L. Niewolak, E. Wessel, L. Singheiser, and W. J. Quadackers, *Journal of Power Sources* **195**, 2010 (7600). <https://doi.org/10.1016/j.jpowsour.2010.06.007>.
31. I. Barin, *Thermochemical Data of Pure Substances*, vol. I Ag-Kr, 3rd ed (VCH Verlagsgesellschaft mbH, New York, 1995),.
32. R. A. Pasternak, M. V. Christensen, and J. Heller, *Macromolecules* **3**, 1970 (366).
33. A. Knizhnik, P. Komarov, B. Potapkin, D. Shirabaykin, A. Sinita, and S. Trepalin, *Minerals* **13**, 2023 (1151). <https://doi.org/10.3390/min13091151>.

Publisher's Note Springer Nature remains neutral with regard to jurisdictional claims in published maps and institutional affiliations.